J. metamorphic Geol., 2003, **21,** 253–268

Strain rates from snowball garnet

C. BIERMEIER AND K. STÜWE
Department of Geology and Palaeontology, Karl Franzens University, Heinrichstr 26, A 8010 Graz, Austria
(kurt.stuewe@uni-graz.at)

ABSTRACT Spiral inclusion trails in garnet porphyroblasts are likely to have formed due to simultaneous growth and rotation of the crystals, during syn-metamorphic deformation. Thus, they contain information on the strain rate of the rock. Strain rates may be interpreted from such inclusion trails if two functions are known: (1) The relationship between rotation rate and shear strain rate; (2) the growth rate of the crystal. We have investigated details of both functions using a garnetiferous mica schist from the eastern European Alps as an example. The rotation rate of garnet porphyroblasts was determined using finite element modelling of the geometrical arrangement of the crystals in the rock. The growth rate of the porphyroblasts was determined by using the major and trace element distributions in garnet crystals, thermodynamic pseudosections and information on the grain size distribution. For the largest porphyroblast size fraction (size $L = 12$ mm) we constrain a growth interval between 540 and 590 °C during the prograde evolution of the rock. Assuming a reasonable heating rate and using the angular geometry of the spiral inclusion trails we are able to suggest that the mean strain rate during crystal growth was of the order of $\dot{\gamma} = 6.6 \times 10^{-14}$ s^{-1}. These estimates are consistent with independent estimates for the strain rates during the evolution of this part of the Alpine orogen.

Key words: grain growth; rotation rate; snowball garnet; strain rate; trace element zoning.

INTRODUCTION

Strain rate is one of the most difficult parameters to extract from deformed metamorphic rocks as it is only indirectly recorded in the thermal, baric, isotopic and textural record of relevant mineral assemblages. Mean strain rates may be determined from cross cutting relationships or bulk palaeogeographic constraints, for example from sea-floor spreading rates (Pfiffner & Ramsay, 1982). However, direct measurements of strain rate in metamorphic rocks are rare. Isotopic dating of strain fringes (Müller *et al*., 2000) and garnet growth zones (e.g. Vance *et al*., 1992; Christensen *et al*., 1994) are among the few examples for which this has been attempted. In principle, strain rate information is also contained in spiral inclusion trails of snowball garnet crystals, if such spiral inclusion trails form by growth of the crystal over a planar fabric during its progressive rotation (Schoneveld, 1977; Passchier *et al*., 1992). Then, snowball garnet crystals may be interpreted in terms of strain rates if two functions are known: (1) The relationship between the rotation rate of the porphyroblast and the shear strain rate of the rock. (2) The growth rate of the crystal through time.

Under ideal conditions, these two functions are reasonably straightforward to constrain. For example, in a rock containing a single porphyroblast in a much softer matrix subject to ideal simple shear, the rotation rate is one half of the shear strain rate (Ghosh & Ramberg, 1976; Simpson & De Paor, 1993). The growth rate of the crystal may be determined by superimposing a known *P–T–t* path on an appropriate thermodynamic pseudosection contoured for mineral modes. By combining growth and rotation rate information, a strain rate may then be inferred.

However, in most rocks, growth and rotation rates are not so easily interpreted. *P–T–t* paths are commonly not well enough known to constrain the temporal evolution of the heating path, and therefore the growth rate. However, even if that is known, there are problems with the relative nucleation history of different grains that make an interpretation of both growth and rotation rates difficult. For example, Fig. 1 shows that crystals and their spiral inclusion trails vary dramatically in size, shape and orientation within a few cm^3 of rock. This indicates that the rates of growth, nucleation and/or rotation have a large spatial variation on small length scales.

Some of problems with the thin section scale variability of growth and rotation rate have recently been addressed. For example, the variability of porphyroblast rotation rate within a single hand specimen was recently discussed by Biermeier *et al*. (2001) and recent advances in the understanding of growth- and nucleation rates were made by Spear & Daniel (1998) and Carlson *et al*. (1995).

In this study some of this information is summarised and expanded in a general way. We also attempt to constrain the nucleation history of snowball garnet crystals by using major and trace element distribution in garnet porphyroblasts. As an example, a

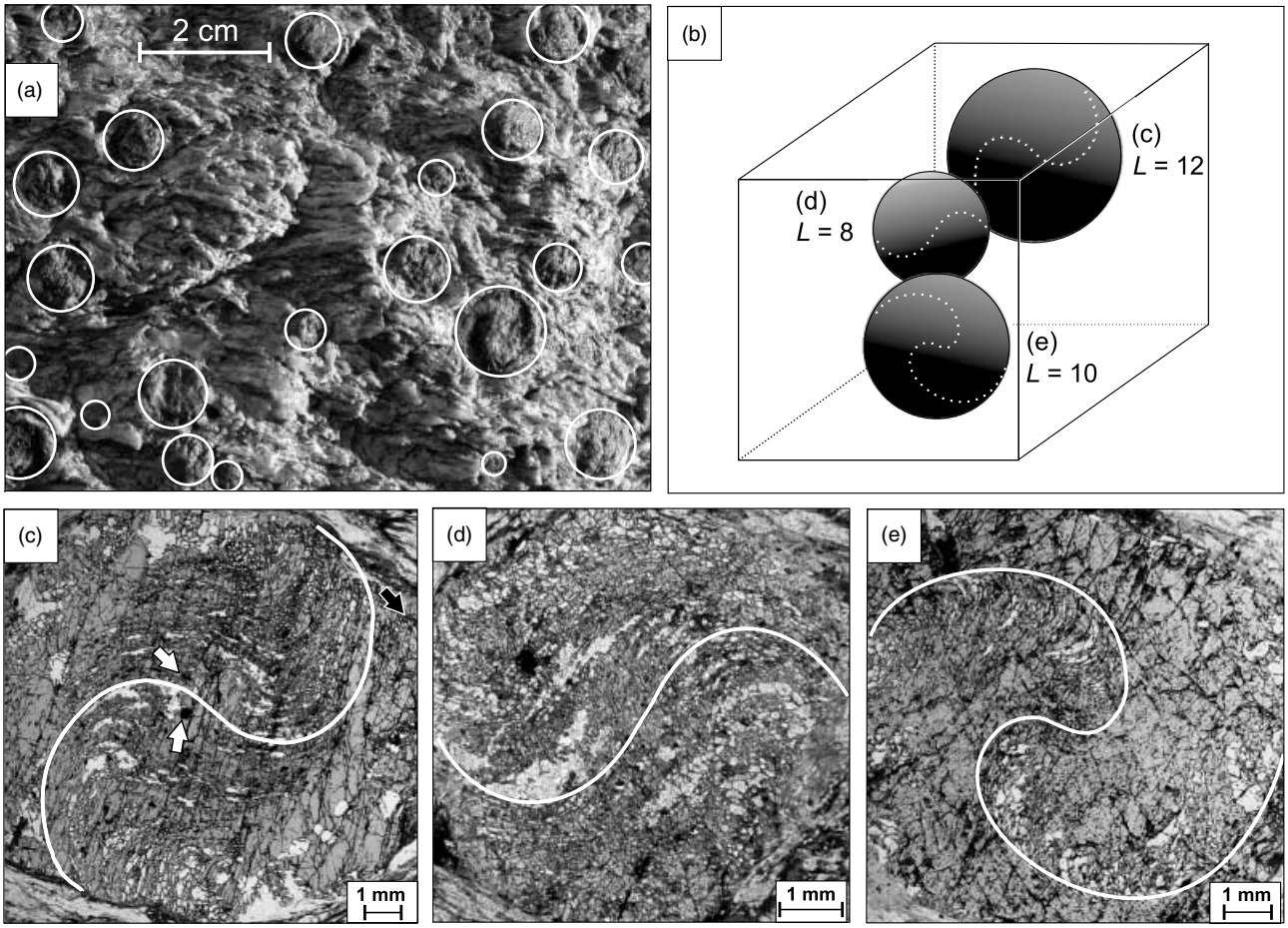

Fig. 1. Examples of spiral inclusion trails in garnet from the Gleinalm complex (Austroalpine nappe complex, eastern Alps, Austria). (a) Photograph of hand specimen showing garnet density and size variation. The stretching lineation is parallel to the scale bar. (b) Cartoon showing the actual 3-D arrangement of the three garnet crystals shown in (c) (d) and (e). The photomicrographs are of thin sections cut central to each of the three garnet crystals (L is the garnet diameter in mm). Note that the inclusion trail in (d) indicates an opposite sense of rotation from that of (c) and (e) and that the tightness of the spirals in (c) and (e) varies. The inclusion trails in the garnet cores (best visible in c) are mostly ilmenite needles (white arrows) and quartz. The larger inclusions in the more massive rims are rutile (dark arrow).

garnetiferous mica schist from the Gleinalm crystalline complex in the Eastern Alps is used. In the later parts of the paper we investigate the potential of snowball garnet crystals to determine strain rates from their spiral inclusion trails. While many of the data used here are potentially subject to large errors, the purpose of this study is to emphasize the enormous potential of petrological data and microtextures for the direct measurement of strain rates.

GROWTH AND ROTATION RATE

Rotation rate

There is no doubt that inclusion trails in porphyroblasts develop coeval with their growth by overgrowing matrix minerals, but there has been some controversy about the interpretation of rotational behaviour of garnet in a deforming matrix as seemingly evident from spiral-shaped inclusion trails. The argument that the foliation in the matrix rotates before being overgrown by the porphyroblast (e.g. Bell *et al*., 1992a, 1992b; Johnson & Bell, 1996; Hickey & Bell, 1999) is in contrast to the argument that inclusion trails record the rotation of porphyroblasts during deformation (e.g. Schoneveld, 1977; Williams & Schoneveld, 1981; Passchier *et al*., 1992; Mancktelow & Visser, 1993). Bell (1985) suggested that porphyroblasts can rotate during simple shear deformation if the shear zone boundaries remain a fixed separation, but argued that no spiral inclusion trails form in such environments. He argued that the formation of spiral inclusion trails is limited to environments where shortening occurs across the shear zone boundaries (e.g. Bell *et al*., 1989).

Despite this controversy, some analytical arguments on the rotation rate of objects in a viscous matrix are undisputed: The rotation rate of an rigid, cylindrical object in a matrix of a Newtonian viscous rheology is given by:

$$\dot{\omega} = \dot{\gamma}/2 \qquad (1)$$

(Rosenfeld, 1970; Ghosh & Ramberg, 1976; Simpson & De Paor, 1993; Fig. 2(a), where $\dot{\omega}$ is the rate of rotation of the object and $\dot{\gamma}$ is the shear strain rate (given by the time derivative of $\gamma = \tan(\psi)$, where ψ is the angular shear strain). Equation (1) is a simplified form of a more general description for the rotation rate of elliptical objects given by Jeffrey (1922). These relationships were confirmed by a

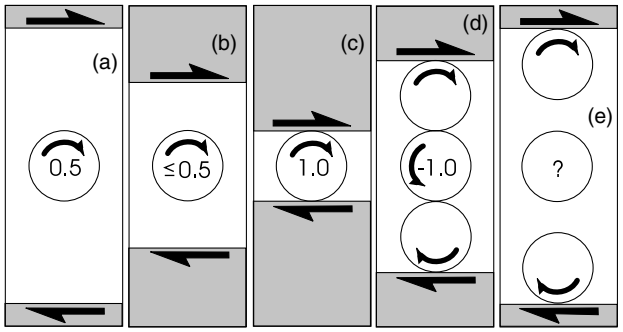

Fig. 2. Cartoon illustrating the range of possible rotation rates of a circular object for different porphyroblast geometries and distances of the boundary conditions. Shaded blocks illustrate the boundaries where dextral simple shear is imposed. Rotation rates for the different scenarios are explained in detail in the text.

range of analytical and experimental studies that have expanded and applied them to the description of porphyroblast behaviour in rocks (e.g. Rosenfeld, 1970; Masuda & Ando, 1988; Masuda & Mochizuki, 1989; Visser & Mancktelow, 1992; Bjornerud & Zhang, 1994; Williams & Jiang, 1999).

However, the rotation rate from eq. (1) may vary if the object is not free to rotate in an infinite matrix, but is confined by boundary conditions at finite distance and if the rheology is nonlinear (Biermeier *et al*., 2001). Both are given in rocks like that shown in Fig. 1(a). In this rock the garnet crystal density is high enough so that some crystals may act as 'effective shear zone boundaries' to other crystals (indicating that they may influence each others rotational behaviour).

Figure 2 illustrates how the proximity of effective boundary conditions may influence the rotational behaviour of porphyroblasts. Figure 2(a) shows a single porphyroblast in an infinite matrix where $\dot{\omega}$ is given by eq. (1) (Jeffrey, 1922; Ghosh & Ramberg, 1976). In contrast, Fig. 2(c) shows a porphyroblast touching the shear zone boundary. It is forced to rotate with a dextral shear motion so that its rotation rate is $\dot{\omega} = \dot{\gamma}$. Figure 2(b) shows the intermediate case in which the distance to the boundaries (e.g. the next porphyroblast) is comparable to the diameter of the porphyroblast itself. Interestingly, the rotation rate is less than 0.5 $\dot{\gamma}$ (Biermeier *et al*., 2001). If several porphyroblasts touch each other (Fig. 2d), the rotation rate of the central porphyroblast may even become negative. As with gearing, the rotation rate is $\dot{\omega} = -\dot{\gamma}$. Similarly, the sense of rotation may also change if crystals are located in different locations with respect to the hinge of a fold (e.g. Visser & Mancktelow, 1992). Finally, Fig. 2(e) shows a schematic cartoon illustrating a case with several porphyroblasts that do not touch each other, as may be representative for a coarse grained rock like that shown in Fig. 1(a). In view of the highly variably rotation rates illustrated in Fig. 2(a–d), it may be concluded that it is difficult to predict the rotation rate for this case.

To illustrate the variability of rotation rate with geometry of the porphyroblast arrangement further, we have numerically calculated rotation rates for different porphyroblast geometries using the FEM package BASIL of Barr & Houseman (1996) (Fig. 3). Numerical techniques and boundary conditions (fixed *v*. constant stress boundary conditions and linear *v*. nonlinear viscous rheologies) are identical to those described by Biermeier *et al*. (2001) and will not be repeated here. Figure 3 illustrates that the rotation rate varies widely between $\dot{\omega} = 0.25\ \dot{\gamma}$ and $\dot{\omega} = 0.75\ \dot{\gamma}$, depending on the number and geometry of the objects. For example, the rotation rate of a single circular inclusion (Fig. 3a) is similar to that of a more or less densely packed geometry of nine objects (Fig. 3f), but very different from that for three, five or seven objects (Fig. 3b,c,d and e, respectively). Also, the rotation rate of the central of three objects depends strongly on the arrangement of the other two objects (compare b and c). In the first case, the rotation rate is $\dot{\omega} < 0.5\ \dot{\gamma}$ and in the second case the rotation rate is much larger than 50% of the shear

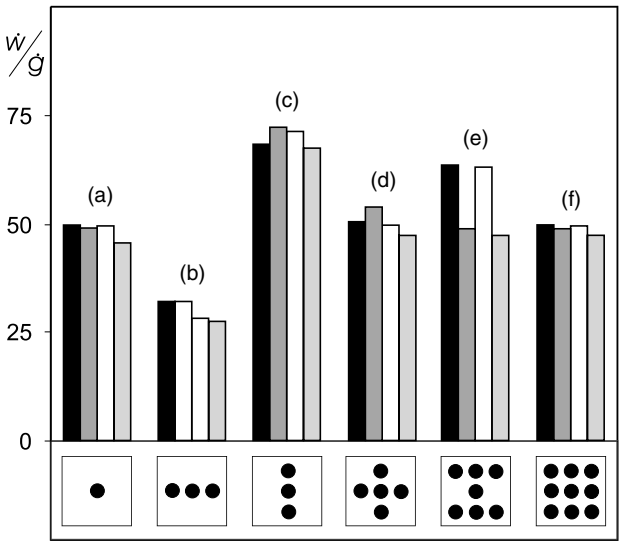

Fig. 3. Numerically modeled rotation rates for six different porphyroblast geometries within a square region. Porphyroblast geometries are shown schematically along the base of the diagram: (a) is for a single circular object (b) and (c) for three objects in different starting geometries (d) for five objects (e) for seven objects and (f) for nine objects. The vertical axis is the rotation rate $\dot{\omega}$ normalized to the shear strain rate $\dot{\gamma}$. Normalized rotation rates are always shown for the central circular object shown in the cartoons at the base. For each geometry, the first two columns (black and dark gray) show normalized rotation rate for linear viscous flow of the matrix. The last two columns (white and light gray) are for nonlinear viscous flow (power law exponent of 3). Black and white columns are for the 'constant stress' boundary conditions of Biermeier *et al*. (2001); dark and light gray columns are for 'fixed plate' boundary conditions. Diagram was calculated with the finite element package BASIL of Barr & Houseman (1996). All details for the numerical method are explained in Biermeier *et al*. (2001).

strain rate. Interestingly, the influence of different boundary conditions and different nonlinearities of viscosity on rotation rate is small (different grey shaded columns in Fig. 3 are of the same length). In conclusion it may be said that the rotation rate of porphyroblasts in linear and nonlinear viscous rocks is roughly 50% of the shear strain rate, if the distance between porphyroblasts is at least half of the porphyroblast diameter. However, the rotational behaviour changes rapidly in response to small changes in the geometry. Depending on geometry, the rotation rate may vary dramatically between $\dot{\omega} = 0.25\,\dot{\gamma}$ and $\dot{\omega} = 0.75\ \dot{\gamma}$.

Growth rate

Rates of crystal growth in metamorphic rocks are difficult to quantify. In principle, volumetric growth rates of crystals may be determined from modal contours on thermodynamic pseudosections (e.g. Stüwe & Powell, 1995), if the rock was in equilibrium at all times and if the *P–T–t* path of the rock is known. Then, the mean growth rate of a crystal $\bar{g}$ of volume V that has grown over a temperature interval ΔT of the *P–T–t* path, which it has crossed at the heating rate $h = dT/dt$ is:

$$\bar{g}(t) = h \cdot V/\Delta T \tag{2}$$

If the crystal is spherical, then the volume in eq. (2) is

$$V = 4(L/2)^3\pi/3, \tag{3}$$

where L is the diameter of the crystal.

However, if not all crystals in the rock nucleated at the same time or are of the same size, then this information is not sufficient: it is additionally necessary to determine the relative times of nucleation and growth of different crystals. These strongly depend on the rate limiting process (e.g. Jones *et al*., 1972; Kretz, 1973; Finlay & Kerr, 1987; Carlson *et al*., 1995). The rate limiting process may either be the transport of matter to the site of porphyroblast growth (diffusion control), or the incorporation of matter into the crystal lattice (interface control). For example, based on radius-rate data, Kretz (1974, 1993) argued for an interface controlled growth, whereas Carlson (1989, 1991) and Denison & Carlson (1997) argued for a diffusion-controlled growth. Spear & Daniel (1998) suggested that both interface-control or diffusion-control may be the rate limiting-process over length scales on the order of the average garnet radius or less. They argued that inhomogeneieties in samples favour garnet nucleation and that therefore garnet crystals have a strongly clustered appearance. Daniel & Spear (1999) concluded that the different rate-limiting mechanisms for garnet growth reflect differences in the thermal, deformational and/or fluid flow history.

In order to determine growth and nucleation rates from element distribution within the crystal this element must meet two criteria. First, the intergranular diffusion during garnet growth must be rapid enough to effectively flatten the chemical potential gradient for that element in the matrix so that rock-wide equilibrium is reached. Second, the intracrystalline diffusion rate of this element must be slow enough to retain the original distribution during growth from core to rim. Many trace elements meet the second criterion well, but it is questionable if they meet the first criterion (Yang & Rivers, 2001; Carlson, 2002). Nevertheless, trace element distribution in garnet crystals has been used to determine the relative times of nucleation of differently sized crystals (e.g. Hickmott *et al*., 1987; Hickmott & Shimizu, 1990; Hickmott & Spear, 1992; Lanzirotti, 1995; Vance & Mahar, 1998; Yang *et al*., 1999; Escuder Viruete *et al*., 2000; Spear & Daniel, 2001). In contrast to trace elements, many major elements meet only the first criterion (except for Mn in low-T garnet growth and Ca below the upper amphibolite facies; Carlson, 2002). Thus, major elements may have significant information in their distribution in rocks where growth zoning is preserved and only a close correspondence between growth rate interpretations on the basis of major and on the basis of trace elements gives a good indication that both criteria are met by the element in question.

In the rest of this paper thermodynamic pseudosections, as well as major and trace element zoning information are used to determine the relative times of nucleation and growth of different crystals. This information is then used with rotation rate information to interpret the strain rate of a rock.

SAMPLE DESCRIPTION

For this study, a highly strained Fe-rich micaschist was chosen from the Gleinalm Complex of the Eastern European Alps that contained abundant snowball garnet porphyroblasts (Fig. 1c,d,e). The rock experienced syn-deformational metamorphism during the Eoalpine metamorphic event at *c*. 90 Ma. Details of the regional geology are described by Neubauer *et al*. (1995), Schuster & Thöni (1996), Thöni & Jagoutz (1993) and Miller & Thöni (1997). A cooling history of this area was constrained by Neubauer *et al*. (1995) and their estimates of heating and cooling rates in the region are used.

The grain size distribution, 3-D topology and mineral chemistry was documented by 80 serial thin sections from two oriented rock samples, $5 \times 5 \times 2$ cm in size (Tables 1, 2 & 3a). Most sections were cut parallel to the mineral lineation (which indicates the transport direction, Fig. 1a), but some were cut in the direction perpendicular to this lineation for complete 3-D orientation. Spacing between individual sections is < 1.0 mm. Garnet volume was determined by analysing scanned thin section images and calculating the area proportion with the software OPTIMAS 6.0. Grain size distribution and the total amount of garnet was additionally constrained by hand picking of crystals from 1125 cm^3 of coarsely crushed sample material. This rock contains about 12–13 vol% garnet and most garnet porphyroblasts are between 1 and 22 mm diameter (Fig. 4). The 13 vol% of garnet is only about a fifth of the maximum possible porphyroblast density of spherical objects in cubic closest packing, indicating that the mean distance between porphyroblasts is roughly twice the porphyroblast radius (Fig. 1a). The size distribution is roughly Gaussian with a clustering of grain size around 11–13 mm and a skew towards smaller grain sizes (Fig. 4a). Spiral inclusion trails of garnet crystals appear continuous and crystals have overall single phase appearance in both chemistry and texture so that we assume that all garnet grew during the Eoalpine metamorphic event. Spiral inclusion trails are best developed on sections cut parallel to lineation, supporting the hypothesis that they developed by crystal growth during the principal fabric and lineation forming deformation event. Later deformation events caused some folding of the sample, which may be seen in sections normal to the lineation, but this later event was not associated with garnet growth and will be of not further concern here.

Garnet grains are divided (somewhat arbitrarily) into three groups of different size, L, which also differ in their major and trace element composition: Group I garnet has a diameter of 15 mm $> L1 >$ 10 mm, group II garnet 10 $> L2 >$ 3 mm, and group III are 1 $< L3 <$ 3 mm (Fig. 4a). The mean grain sizes of the three groups are $\bar{L}_1 = 12$ mm, $\bar{L}_2 = 7$ mm and $\bar{L}_3 = 2$ mm (Table 3a). Clearly, the growth of the three different size groups must not have occurred in the same time interval. Figure 4(b) shows three different end member scenarios of the possibly growth relationships between the three size groups. They are: (1) Garnet from all three groups may have grown over the same interval of the P–T–t path, but with different growth rates (Fig. 4bI). (2) All garnet crystals may have nucleated at the same time but terminated growing in proportion to their size (Fig. 4bII). (3) Garnet from all three groups may have grown at the same rate and terminated growing at the same time, but nucleated at different times (Fig. 4bIII). These three scenarios are separated on the basis of porphyroblast composition as discussed below.

Petrography and mineral chemistry

The rock has an assemblage quartz–muscovite–paragonite–biotite–garnet–plagioclase–chlorite. Ilmenite, rutile, monazite and zircon occur as accessories. Details of the mineral chemistries are shown in Tables 1 and 2.

Garnet

Garnet is rich in spiral-aligned inclusions of predominantly quartz and some oxides. However, inclusion style, density and inclusion mineralogy change from core to rim. In garnet of groups I and II cores abundant small ilmenite needles and larger quartz inclusions form a dense intergrowth with garnet defining the spiral trail. Rims have substantially fewer inclusions and have a more massive appearance. These rims contain concentrically oriented rutile inclusions. Group III garnet contains no ilmenite inclusions and is similar to the rims of larger group I and II garnet. Concentrically oriented rutile inclusions may or may not occur. Along their rims, most garnet crystals are partially replaced by chlorite, muscovite, biotite, quartz and plagioclase, but these retrograde replacements do not affect the geometry of the spiral inclusion trails. Interestingly, garnet of the large size groups I and II are typically more resorbed than group III crystals. Micro-cracks in the larger garnet crystals are filled with chlorite, quartz and biotite. All textural and chemical changes discussed below are for sections cut through the centres of crystals.

Group I garnet crystals have a continuous decrease in $X_{Fe} = Fe/(Fe + Mg)$ from core to rim from 0.95 to *c*. 0.85 (Fig. 5a, Table 1). However, they have pronounced bell-shaped zoning profiles in both X_{Alm} and X_{Grs} (defined as $X_{Alm} = Fe/(Fe + Mg + Ca + Mn)$ and $X_{Grs} = Ca/(Ca + Fe + Mg + Mn)$). From core to rim, X_{Alm} first increases from 0.63 to 0.74 and then decreases to 0.66 in the outermost 10% of the rim. Correspondingly, X_{Grs} decreases from 0.26 to 0.17 in the central third of the crystals and is largely constant in the outer rims. $X_{Pyp} = Mg/(Mg + Fe + Ca + Mn)$ increases continuously from core to rim from 0.03 to *c*. 0.12 and there is a symmetric outward decrease of $X_{Spss} = Mn/(Mn + Fe + Mg + Ca)$ from 0.09 to 0.01. Smaller garnet crystals have no bell-shaped zoning profiles and have significantly lower Mn core compositions than group I garnet. Group II (Fig. 5b) show more or less constant X_{Alm} of *c*. 0.75 and continuously decreasing contents of X_{Grs}, X_{Spss} and X_{Fe} from 0.19 to 0.12, 0.035–0.005 and 0.94–0.84, respectively. X_{Pyp} increases from core to rim from 0.06 to 0.14. Group III garnet has the lowest Mn contents with X_{Spss} *c*. 0.005 (Fig. 5c). There is a slight decrease in the X_{Grs} content from core to rim from 0.12 to 0.10. X_{Alm} and X_{Fe} show a more pronounced decrease from 0.74 to 0.68 and 0.84–0.77, respectively. X_{Pyp} increases from 0.15 to 0.2.

Selected trace element distributions are similar for group I and II, but very different for group III garnet crystals (Fig. 6a,b, Table 2). Interestingly, the concentrations of rare earth elements in the rims of group I and II garnet is similar to those in the cores of group III garnet crystals (Fig. 6c). In garnet of group I and II, Dy, Ho, Er, Tm, Yb and Lu decrease from core to rim. Eu, Gd and Tb contents increase from core to rim

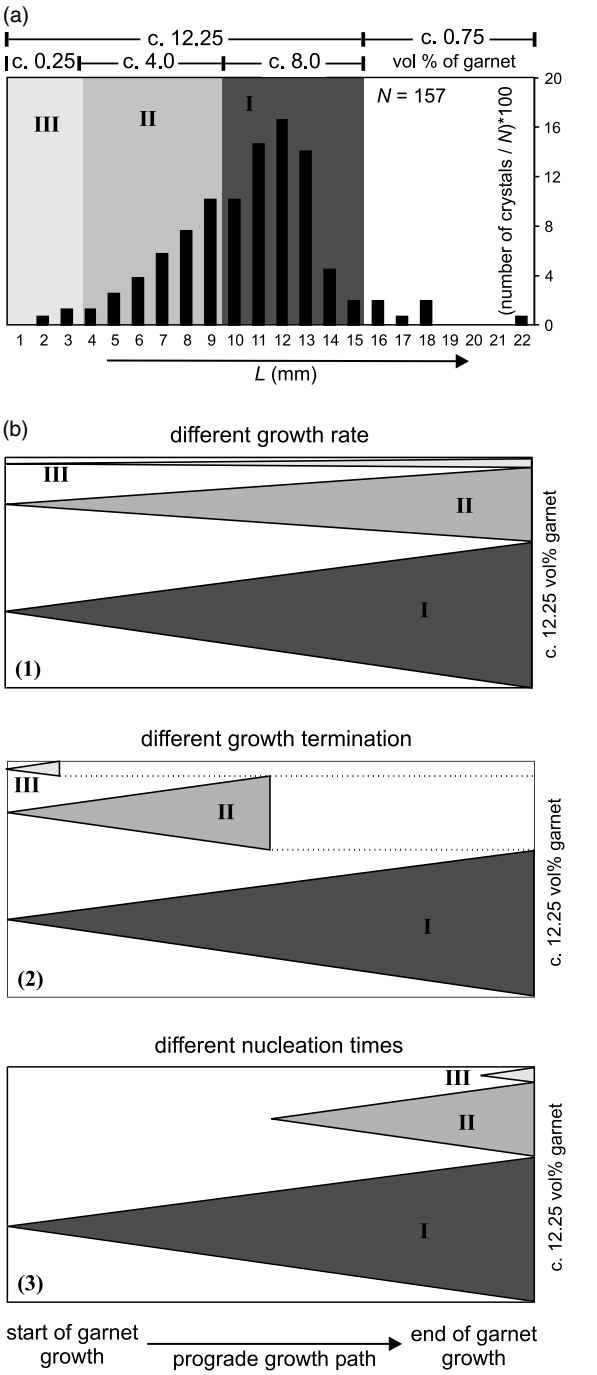

Fig. 4. (a) Grain size distribution of garnet crystals in the sample under investigation. *N* is the total number of counted grains and *L* is grain size. The gray shaded background indicates the grouping of garnet used in the text and in subsequent figures. Volumetric garnet proportions of the different groups are shown along the top of the diagram. The total volume of garnet in the rock is 13 vol%. (b) Cartoon illustrating different possible end members of the relative growth and nucleation history of the three different garnet size groups. (1) Different growth rate; (2) different growth termination and (3) different nucleation times. More details on these three scenarios in text. The shading for the three different size groups correlates to that used in Figs 5, 6(d) & 8(b).

Table 1. Representative microprobe data for garnet of groups I, II and III and matrix minerals. Subscripts refer to the three different size groups of garnet. Superscripts refer to c = contact with garnet, m = matrix phase.

Mineral Position	Grt_I core	Grt_I rim	Grt_{II} core	Grt_{II} rim	Grt_{III} core	Grt_{III} rim	Pl_I rim^c	Pl_{II} rim^m	Bt rim^c	Bt rim^m	Pg rim^m	Pg rim^c	Ms rim^m	Ms rim^c	Chl rim^m
Wt% oxides															
SiO_2	36.88	37.85	36.83	37.23	37.44	37.93	62.06	64.35	35.34	35.7	48.06	48.14	48.17	48.81	26.43
TiO_2	0.17	0.2	0.11	0.2	0.08	n.d.	n.d.	n.d.	0.64	0.32	0.24	0.19	0.63	0.71	n.d.
Al_2O_3	20.82	21.47	20.94	21.41	20.76	21.36	23.63	22.26	19.49	16.66	39.23	38.65	32.56	30.97	21.81
FeO	29.4	29.9	33.18	32.26	33.48	31.53	0.47	n.d.	17.33	23.41	0.17	1.69	1.52	1.74	21.4
MnO	3.32	0.57	1.28	0.31	0.28	0.16	n.d.	n.d.	0.16	0.32	n.d.	0.3	n.d.	n.d.	n.d.
MgO	1.28	3.48	1.28	3.55	3.78	5.45	n.d.	n.d.	12.03	8.7	n.d.	n.d.	1.87	2.86	17.77
CaO	8.08	6.74	6.06	5.09	4.04	3.68	5.69	3.68	n.d.	n.d.	0.2	0.14	n.d.	n.d.	n.d.
Na_2O	n.d.	n.d.	n.d.	n.d.	n.d.	n.d.	8.37	9.35	0.06	0.044	5.76	6.09	0.96	1.15	n.d.
K_2O	n.d.	n.d.	n.d.	n.d.	0.01	n.d.	0.1	0.08	9.59	9.35	1.21	1.74	9.34	9.31	n.d.
Total	99.95	100.21	99.68	100.05	99.87	100.11	100.32	99.72	94.64	94.504	94.87	96.94	95.05	95.55	87.41
No. Oxygen	12	8	12	12	12	12	8	8	11	11	11	11	11	11	14
Si	2.95	2.97	2.96	2.94	2.99	2.96	2.73	2.84	2.67	2.79	3.06	3.04	3.19	3.21	2.71
Ti	0.01	0.01	0.01	0.01	0.00	0.01	0.00	0.00	0.04	0.02	0.01	0.01	0.03	0.03	0.00
Al	1.96	1.99	1.99	2.00	1.95	1.99	1.23	1.16	1.73	1.54	2.95	2.87	2.55	2.40	2.64
Fe^{3+}	0.06	0.06	0.06	0.06	0.06	0.06	0.03	n.d.	0.12	0.09	0.00	0.02	0.00	0.05	0.04
Fe^{2+}	1.97	1.96	2.23	2.13	2.18	2.23	0.02	n.d.	0.97	1.44	0.01	0.09	0.08	0.10	1.84
Mn	0.22	0.04	0.09	0.02	0.02	0.09	n.d.	n.d.	0.01	n.d.	n.d.	0.02	n.d.	n.d.	n.d.
Mg	0.15	0.41	0.15	0.42	0.45	0.15	n.d.	n.d.	1.35	1.01	n.d.	n.d.	0.18	0.30	2.72
Ca	0.69	0.57	0.52	0.43	0.35	0.52	0.27	0.17	n.d.	n.d.	0.01	0.01	n.d.	n.d.	n.d.
Na	n.d.	n.d.	n.d.	n.d.	n.d.	n.d.	0.71	0.80	0.01	0.01	0.71	0.74	0.12	0.15	n.d.
K	n.d.	n.d.	n.d.	n.d.	0.00	n.d.	0.01	0.00	0.92	0.93	0.10	0.14	0.79	0.78	n.d.
Total	8.01	8.03	8.01	8.01	8.00	8.01	5.00	4.97	7.82	7.83	6.85	6.94	6.94	7.02	9.95
X_{Alm}	0.65	0.66	0.74	0.71	0.73	0.74									
X_{Pyp}	0.05	0.14	0.05	0.14	0.15	0.05									
X_{Grs}	0.23	0.19	0.17	0.14	0.12	0.17									
X_{Spss}	0.07	0.01	0.03	0.01	0.01	0.03									

in the central half of the crystals and are constant in the rim (Fig. 6a). Group III garnet crystals have slightly lower concentrations of most elements than the larger garnet crystals and display little zoning with respect to the rare earth elements (Fig. 6b). Of other trace elements, Y concentrations of group I and II typically decrease from about 1000 p.p.m. in the cores to detection limit near the rims. Y concentrations of group III garnet crystals decrease from 100 p.p.m. in the core to detection limit near the rim (Fig. 6d). Li, Sc, Ti, V, Cu and Ga show similar trends to Y and Co, Ni, Cu as well as Zn show opposite trends to Y. However the trends of these elements are very scattered and are therefore not discussed here.

Table 2. Representative trace element data for garnet crystals of groups II and III. Group I is largely similar to group II.

	Core II	Rim II	Core III	Rim III
p.p.m.				
Li	97.573	45.242	28.080	25.287
Sc	306.568	50.186	63.739	51.953
Ti	747.297	551.756	399.048	393.003
V	118.212	83.378	69.131	63.265
Cr	102.779	147.275	131.016	376.400
Mn	22461.406	4266.658	1499.319	1529.202
Co	15.379	39.660	19.612	32.038
Ni	74.474	29.296	14.371	44.213
Cu	37.858	2.200	6.232	4.265
Zn	143.603	215.719	117.979	158.440
Ga	50.735	9.385	6.264	6.427
Y	637.848	61.267	59.014	33.250
Zr	3.081	5.598	7.562	4.270
Eu	1.508	3.376	3.350	2.072
Gd	12.278	22.259	16.651	14.197
Tb	5.327	2.995	3.488	2.852
Dy	56.763	16.236	15.495	11.700
Ho	18.255	2.373	2.710	2.316
Er	65.531	5.769	6.534	5.348
Tm	12.871	1.259	1.180	1.068
Yb	106.442	5.564	8.240	8.031
Lu	13.860	1.114	1.526	1.561

Matrix and inclusion minerals

In the matrix, muscovite is intercalated and aligned with paragonite in a well defined foliation. Muscovite has Si contents from 3.24 to 3.26 c.p.f.u. (11 O) and *c*. 3.04 c.p.f.u. (11 O) for paragonite. The K/(K + Na) ratio is between 0.85 and 0.92 c.p.f.u. (11 O) for muscovite and between 0.10 and 0.16 c.p.f.u. (11 O) for paragonite (Table 1). The total white mica content is *c*. 20 vol%. Intergrowth of muscovite and biotite (*c*. 12 vol%) is common and they form a reaction texture to chlorite. Rim compositions of biotite vary between $X_{Fe} = 0.37$ and $X_{Fe} = 0.60$ and TiO_2 is between 0.01 and 0.10 c.p.f.u (11 O). Mn is < 0.002 c.p.f.u (11 O) and Na is between 0.006 and 0.034 c.p.f.u (11 O). Plagioclase (*c*. 4 vol%) occurs as recrystallized grains in the pressure shadows around garnet and as clasts with recrystallization rims in the matrix. Plagioclase does not occur as an inclusion phase within garnet. Together they show a wide variation in anorthite content ($X_{An} = 0.18$–0.27). Chlorite (*c*. 4 vol%) occurs

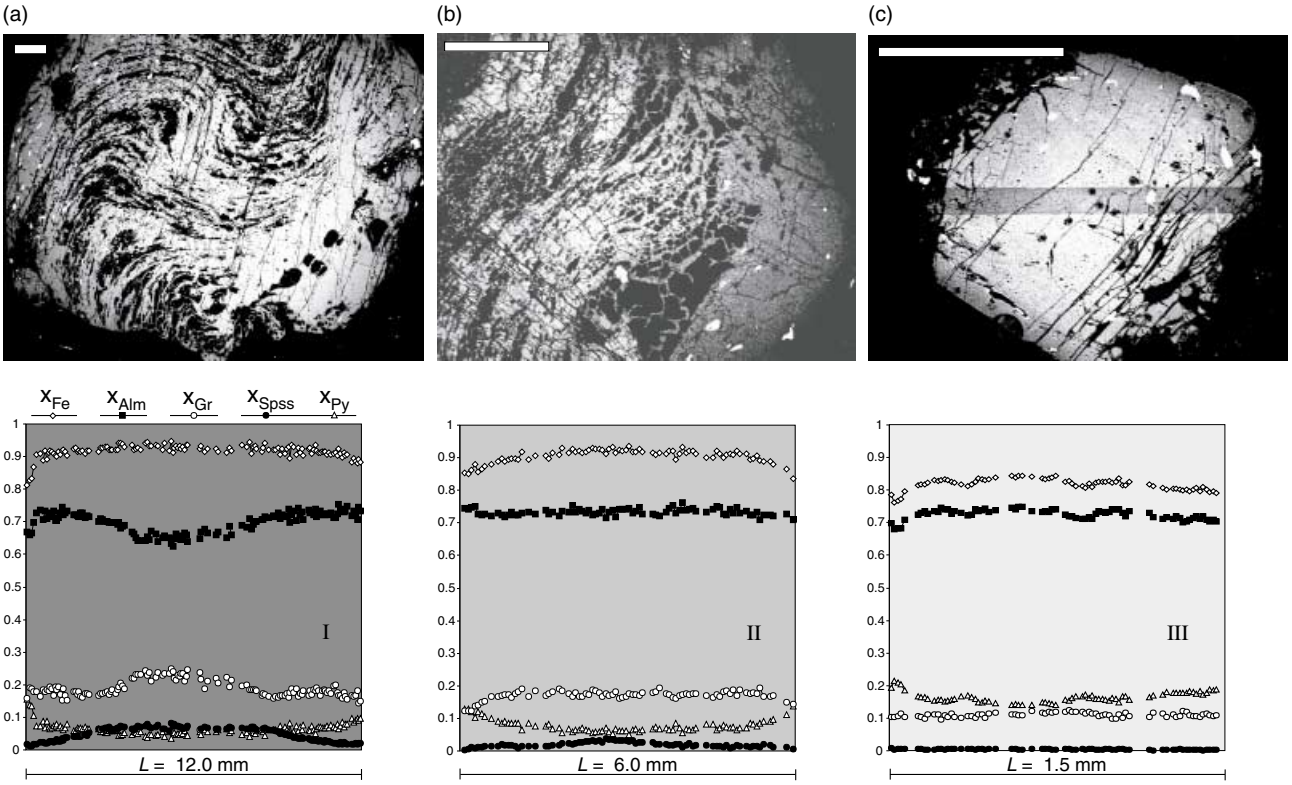

Fig. 5. Compositional maps (top row) and zoning profiles (bottom row) for one garnet crystal from each size group. The two diagrams in (a) are representative for group I (b) for group II, and (c) for group III. The compositional maps are back scattered images and show clearly that the compositional zoning of the crystals is concentric. The individual maps for Ca, Fe, Mg and Mn do all show that same information as may be read from the back scattered images and are available from the authors. The scale bar is 1 mm in each picture. All three profiles are for central sections through crystals. The holes in (c) are from laser ablation ICPMS work performed for Fig. 6. The background shading for the three different size groups correlates to the shadings in Figs 4,6(d) & 8(b).

in the matrix as single crystals up to 5 mm in size. However, the amount and distribution of chlorite can vary significantly on thin section scale. Pressure shadows around garnet are always of chlorite but do not show a preferred orientation. Muscovite and biotite are replaced by chlorite and cracks in garnet are filled with chlorite. The X_{Fe} ratio of chlorite is *c*. 0.4. More than 40 vol% of the rock is quartz. Accessory ilmenite, rutile and monazite also occur. As in the garnet, both ilmenite and rutile occur as accessory phases in the

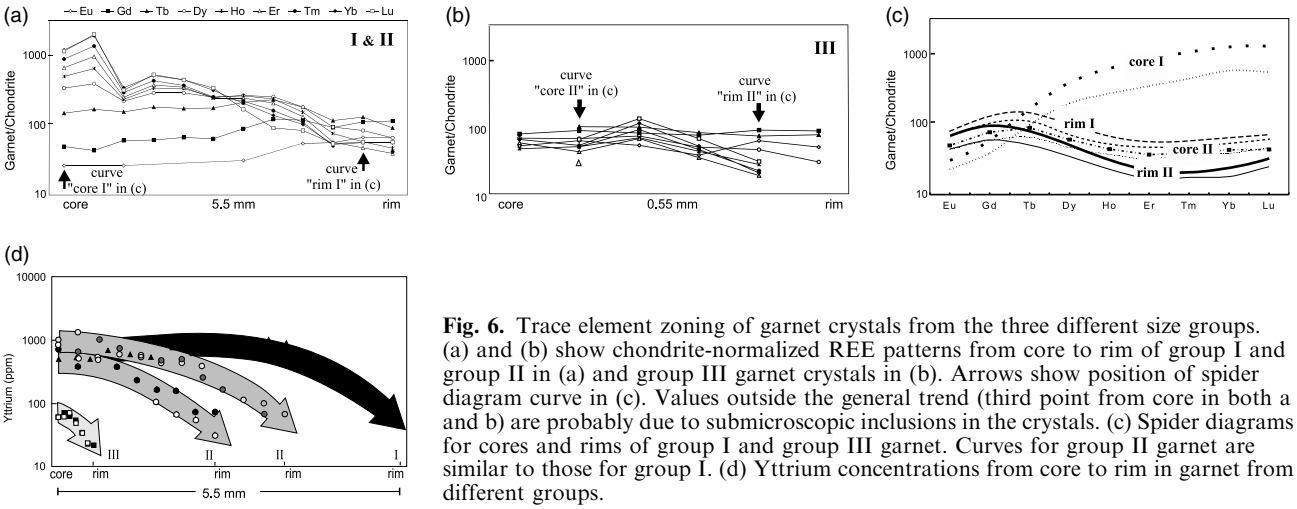

Fig. 6. Trace element zoning of garnet crystals from the three different size groups. (a) and (b) show chondrite-normalized REE patterns from core to rim of group I and group II in (a) and group III garnet crystals in (b). Arrows show position of spider diagram curve in (c). Values outside the general trend (third point from core in both a and b) are probably due to submicroscopic inclusions in the crystals. (c) Spider diagrams for cores and rims of group I and group III garnet. Curves for group II garnet are similar to those for group I. (d) Yttrium concentrations from core to rim in garnet from different groups.

matrix. The ilmenite crystals show an increase in the core to rim composition with 0.42–2.35 wt% MnO, whereas Fe and Ti decrease (Fe more than Ti). This matrix ilmenite largely occurs as narrow overgrowths on rutile. We therefore interpret this ilmenite to be part of the retrograde evolution and infer as the peak paragenesis Grt–Ms–Pg–Bt–Chl–Pl–Qtz–Rt–H_2O (mineral abbreviations after Kretz, 1983).

THERMODYNAMIC MODELLING OF GARNET GROWTH

In order to model garnet growth and growth rate, a three step procedure was used. (1) A thermodynamic pseudosection is calculated based on the known bulk composition. (2) The pseudosection information is used in comparison to major element composition to construct a *P–T* path. (3) Major and trace element zoning of differently sized crystals is used to constrain the relative times of nucleation and estimate the growth rate using known timing constraints.

Pseudosection and *P–T–t* path

The volumetric garnet growth is constrained by constructing a thermodynamic pseudosection for the bulk rock composition. Bulk compositions were obtained (1) by XRF analysis (listed in the caption of Fig. 7) and (2) by point counting mineral modes and converting those into a bulk composition using THERMOCALC (Powell & Holland, 1988) with the procedure described by Stüwe & Powell (1995). In order to test the robustness of the pseudosection to changes in bulk composition, a series of pseudosections were constructed for both bulk compositions (also testing for changes in response to changes of Na_2O–CaO and FeO–MgO ratios) (Biermeier & Stüwe, unpublished information). Pseudosections for both bulk compositions were calculated for a series of successively more complicated chemical systems including K_2O–FeO–MgO–Al_2O_3–SiO_2–H_2O (KFMASH), Na_2O–CaO–KFMASH (NCKFMASH) and TiO_2–NCKFMASH using THERMOCALC. In view of the principal aim of this paper, we refrain from a more detailed discussion of the results from the pseudosection calculations here, and present in Fig. 7 only one pseudosection from calculations in the model system TiO_2–NCKFMASH. We are confident that this pseudosection reflects the effective bulk composition of the investigated sample well, because it is consistent with a range of textural observations (see below). The influence of Mn on the strain rate estimates derived from this pseudosection is discussed below. For a more detailed discussion of the problems associated with the determination of this 'effective bulk composition' readers are referred to Marmo *et al.* (2002), Zeh (2001) and Stüwe (1997).

The pseudosection is largely consistent with the mineralogy of the investigated sample. Within the

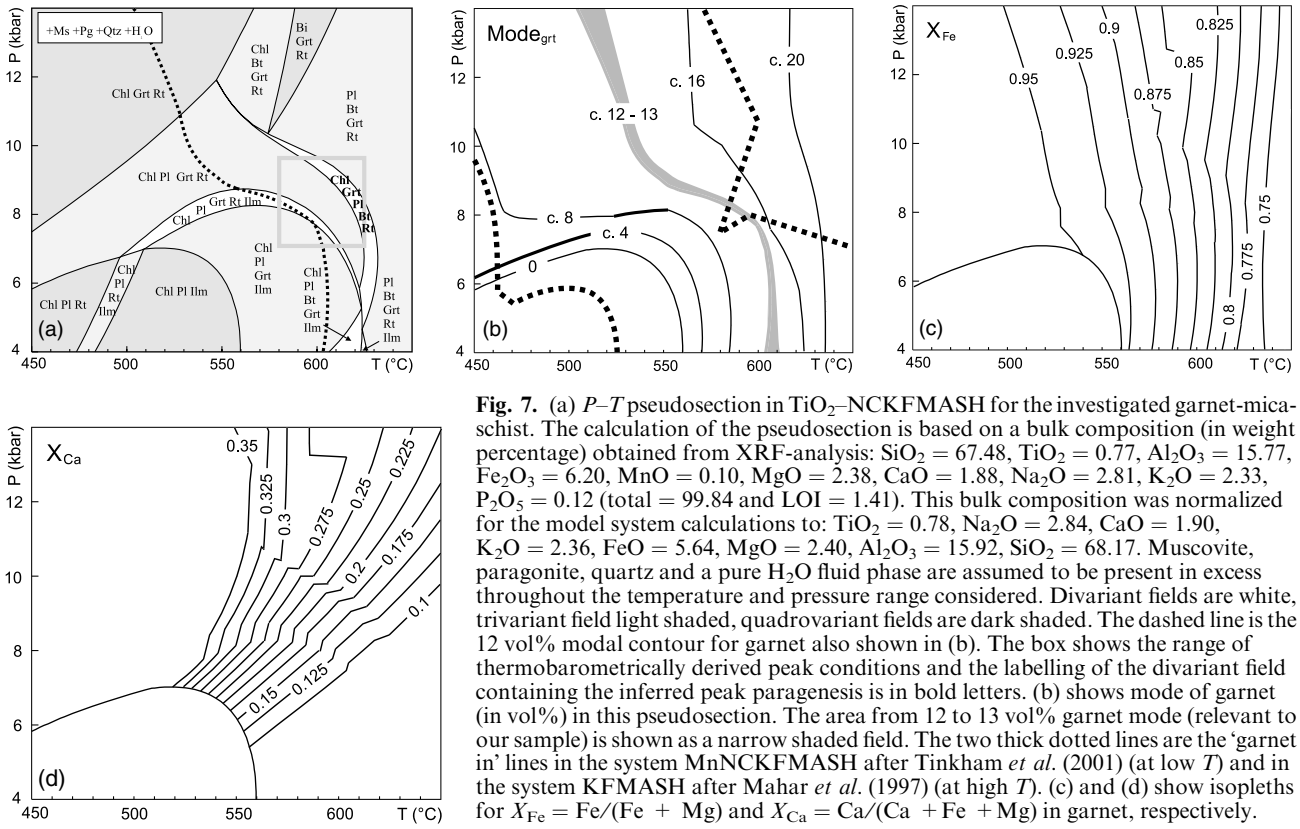

Fig. 7. (a) *P–T* pseudosection in TiO_2–NCKFMASH for the investigated garnet-mica-schist. The calculation of the pseudosection is based on a bulk composition (in weight percentage) obtained from XRF-analysis: $SiO_2 = 67.48$, $TiO_2 = 0.77$, $Al_2O_3 = 15.77$, $Fe_2O_3 = 6.20$, MnO = 0.10, MgO = 2.38, CaO = 1.88, $Na_2O = 2.81$, $K_2O = 2.33$, $P_2O_5 = 0.12$ (total = 99.84 and LOI = 1.41). This bulk composition was normalized for the model system calculations to: $TiO_2 = 0.78$, $Na_2O = 2.84$, CaO = 1.90, $K_2O = 2.36$, FeO = 5.64, MgO = 2.40, $Al_2O_3 = 15.92$, $SiO_2 = 68.17$. Muscovite, paragonite, quartz and a pure H_2O fluid phase are assumed to be present in excess throughout the temperature and pressure range considered. Divariant fields are white, trivariant field light shaded, quadrovariant fields are dark shaded. The dashed line is the 12 vol% modal contour for garnet also shown in (b). The box shows the range of thermobarometrically derived peak conditions and the labelling of the divariant field containing the inferred peak paragenesis is in bold letters. (b) shows mode of garnet (in vol%) in this pseudosection. The area from 12 to 13 vol% garnet mode (relevant to our sample) is shown as a narrow shaded field. The two thick dotted lines are the 'garnet in' lines in the system MnNCKFMASH after Tinkham *et al.* (2001) (at low *T*) and in the system KFMASH after Mahar *et al.* (1997) (at high *T*). (c) and (d) show isopleths for $X_{Fe} = Fe/(Fe + Mg)$ and $X_{Ca} = Ca/(Ca + Fe + Mg)$ in garnet, respectively.

model system TiO_2–NCKFMASH the peak assemblage inferred above is divariant and is stable in the bold labelled field on Fig. 7(a). The modal contour for 12% garnet (dashed line in Fig. 7a) passes this field at somewhat lower temperature. We suggest that this is because some porphyroblasts are partially resorbed and the observed garnet mode is therefore slightly below the peak garnet mode. The position of the peak divariant field is consistent with average *P–T* calculations using matrix phases and garnet rim compositions (from all three size groups). These give *c*. 580–625 °C and 7.1–9.7 kbar.

The prograde *P–T* evolution was constrained using the zoning profiles of garnet. Intersections of X_{Ca} and X_{Fe} contours from Fig. 7(c, d) were constructed for each data point in Fig. 5 and are plotted in Fig. 8(a). They indicate that garnet growth commenced at roughly 540 °C and 6.5 kbar. The prograde *P–T* evolution then appears to have evolved roughly linearly with a *T–P* gradient of 45 °C kbar^{-1} to highest *P–T* conditions at *c*. 630 °C and 8.5 kbar (Fig. 8a). Pressure estimates using the Gd/Dy barometer of Bea *et al.* (1997) give a somewhat higher pressure for the range for the prograde evolution (Fig. 8b). They indicate first garnet growth around 4 kbar and final growth for group III garnet crystals around 14 kbar (Fig. 8b). In summary, peak temperature estimates using different methods are between 625 and 630 °C (average *P–T* calculations v. pseudosection estimates) and peak pressure estimates range between 9 and 14 kbar. Fortunately, the large variation in the peak pressure estimates is of no concern here as modal garnet contours are largely pressure-independent in the considered temperature range (Fig. 7b).

The estimated prograde evolution is consistent with qualitative predictions of the pseudosection shown in Fig. 7(a). There, ilmenite is predicted to be the dominant oxide below the divariant field Chl–Pl–Grt–Rt–Ilm at around 8 kbar and rutile above it. The transition from ilmentite to rutile occurs at about 10% garnet, which is consistent with the observations that only the outer garnet rims contain rutile inclusions (Fig. 1). The integrated best estimate for the prograde *P–T* evolution is shown in Fig. 8(c).

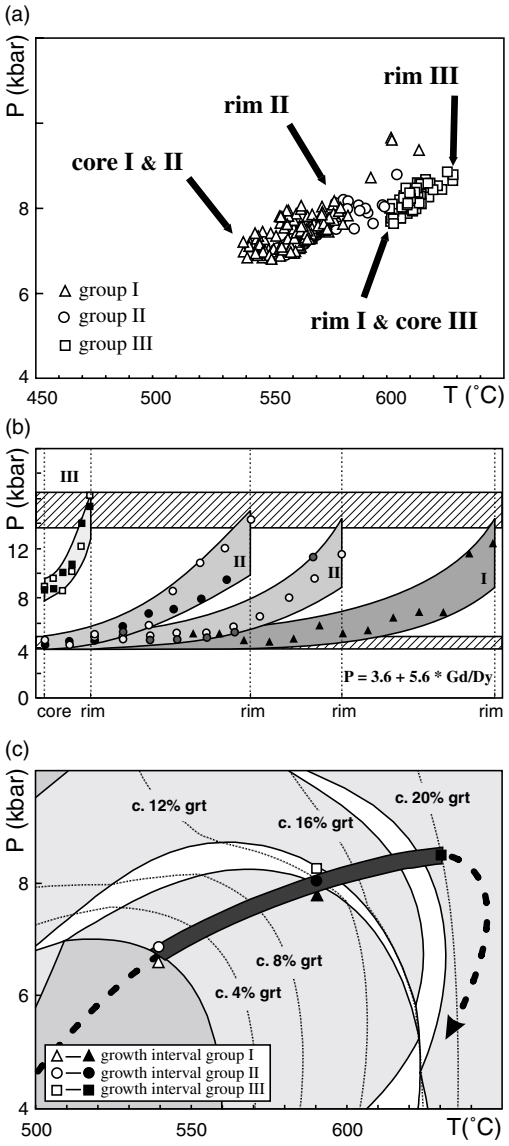

Fig. 8. Pressure estimates and *P–T* path of the investigated sample. (a) shows the prograde *P–T* evolution as estimated from garnet zoning profiles shown in Fig. 5. The data points were obtained from the intersections of the X_{Fe} and X_{Ca} contours shown in Fig. 7 (note that this involves slight conversion from X_{Gr} to X_{Ca}). Triangles, circles and rectangles are for garnet from group I, II and III, respectively. (b) Prograde *P–T* evolution of garnet as estimated with the Gd/Dy barometer of Bea *et al.* (1997). Symbols correspond to those in (a). Note that there are data from two different crystals from size group II. Open and filled symbols are from more or less perpendicular profiles in the same crystal. Shaded overlayed bars highlight the different size groups. The horizontal bars show that all three size groups terminated their growth at similar pressures, but that only group I and II nucleated at the same pressure, while group III nucleated at higher *P*. (c) The prograde *P–T* path of the sample under investigation as obtained from the data discussed in Fig. 8(a,b) and average *P–T* estimates. The *P–T* path is superimposed on part of the pseudosection from Fig. 7(a). Symbols along the *P–T* path indicate our best estimates of the times of nucleation and growth termination of the three different size groups (white for nucleation, black for growth termination). Symbols correspond to those used in Fig. 8(a,b).

Growth and nucleation rates

In the previous section it was established that 12–13 vol% garnet in the rock grew along the prograde *P–T* path of the sample between 540 °C and 625–630 °C indicating a mean garnet growth of *c*. 0.14 vol% per 1 °C. In this section the relative times of nucleation and growth are detailed for the three different crystal size groups (some end member scenarios were illustrated in Fig. 4b). We emphasise that all further interpretation is based on the basic premise that the rock matrix has been in equilibrium at all times so that no overstepping of reactions has caused delays of garnet growth relative to the temperature evolution.

Table 3. Growth parameters and strain rate calculations. (a) shows the growth parameters of the three different size fractions. Volumes, V, were calculated using eq. (3). (b) and (c) show strain rate calculations in (b) for constant volumetric growth rate (as illustrated in Fig. 9b) and in (c) for constant radial growth rate (not illustrated). The rotation rate and strain rate in the last row are the mean values calculated from the total angular change of 299° in 5 Myr. All other parameters are explained in text and the caption of Fig. 9.

Group	vol. (%)	$\bar{L}$ (mm)	ΔT (°C)	V (mm^3)	$\bar{g}\,(T)$ (mm^3/°C)	h (°C/Myr)	$\bar{g}(t)$ (mm^3/Myr)
I	8	12	50	905	18	10	180
II	4	7	50	180	3.6	10	36
III	0.25	2	40	4	0.1	10	1

(b) Strain rate calculation: constant volumetric growth.

t (Myr)	$R_{(t)}$ (mm)	Δt (Myr)	$\Delta\alpha$ (°)	$\dot{\omega}$ (rad/Myr)	$\dot{\gamma}$ (rad/Myr)	$\dot{\gamma}$ (rad/s)
0.25	2.2	0.25	56	3.92	7.84	2.5×10^{-13}
1	3.5	0.75	84	1.96	3.92	1.2×10^{-13}
2	4.4	1	76	1.33	2.66	8.4×10^{-14}
3	5.1	1	35	0.61	1.22	3.9×10^{-14}
4	5.6	1	18	0.31	0.62	2.0×10^{-14}
5	6.0	1	30	0.52	1.04	3.3×10^{-14}
Total	6.0	5	299	1.04	2.08	6.6×10^{-14}

(c) Strain rate calculation: constant radial growth.

t (Myr)	$R_{(t)}$ (mm)	Δt (Myr)	$\Delta\alpha$ (°)	$\dot{\omega}$ (rad/Myr)	$\dot{\gamma}$ (rad/Myr)	$\dot{\gamma}$ (rad/s)
1.66	2	1.66	56	0.59	1.18	3.7×10^{-14}
3.32	4	1.66	126	1.32	2.64	8.4×10^{-14}
4.98	6	1.66	117	1.23	2.46	7.8×10^{-14}
Total	6.0	4.98	299	1.05	2.1	6.7×10^{-14}

For the interpretation below we use (1) trace element distributions, in particular yttrium concentrations (Fig. 6d) and Gd/Dy geobarometry (Fig. 8b), (2) major element distribution (Fig. 5) and (3) geobarometry, geometry of inclusion trails (Fig. 1c–e) and qualitative petrographic estimates in comparison with contoured pseudosection information (Fig. 7). The close correspondence between our interpretation presented below on the basis of trace and that on the basis of major element data indicates that both selected major and trace elements appear to meet the necessary criteria discussed in the conceptual section on growth rate above.

The Y distribution has been previously used to measure growth rates (Lanzirotti, 1995). The growth of group I and II crystals began and terminated at the same Y concentration (Fig. 6d), but group I grew at constant Y concentration for the first part of their evolution. This may be interpreted in two ways. (1) Group I and II crystals may have nucleated and terminated growth at the same time, but grown at different rates (group I grew more rapidly). (2) Group I may have nucleated first and grown for two thirds of their size, before the additional nucleation of group II began to deplete the Y concentration of the matrix. The smallest garnet crystals (group III) have significantly lower Y core concentrations than the other two size groups, indicating that they may have nucleated only in the final stages of group I and II garnet growth and group III growth outlasted that of the other two groups. This interpretation is supported by the Gd/Dy distribution (and calculated pressures therefrom) (Fig. 8b). However, there are a range of problems with group III garnet crystals that defy any certain interpretation of this group and we will therefore not discuss them further (e.g. Why is group III garnet not resorbed? Why does there appear to be a discrete group III nucleation event much later than group I and II nucleation?, etc.).

Major element concentrations are consistent with the interpretation based on trace elements. For reasons discussed above, Mn and Ca are particularly useful to investigate growth histories of garnet crystals (Carlson, 2002), but even Fe and Mg – in all but the smallest size group – show zoning profiles that indicate that information on the growth history is at least partially retained (Fig. 5). Thus, the core concentrations of all four major cations may be used to discriminate between case (3) and cases (1) and (2) on Fig. 4. Correspondingly, rim concentrations may be used to discriminate between case (2) and cases (1) and (3). Mn rim concentrations are similarly low in all three garnet size groups suggesting that they may have terminated their growth at the same time (cases 1 or 3 on Fig. 4). In contrast, both Ca and Mn in the garnet cores are successively lower with decreasing grain size, suggesting that they

nucleated at successively later stages (case 3 on Fig. 4). We therefore suggest that case (3) on Fig. 4 best reflects that growth history of the three size groups, although groups I and II may have nucleated at the same time.

The intersections of X_{Fe} and X_{Ca} contours from Fig 7(b, c) may be used to confirm and quantify this qualitative interpretation. These intersections are shown in Fig. 8(a) and indicate that garnet crystals of size groups I and II grew during similar intervals of the *P–T* path: The growth interval is interpreted to lie between 6.5 kbar at 540 °C and just above 8 kbar at 590–600 °C. This gives a growth interval of 50–60 °C for both groups I and II. Size group III commenced growth in the last stages of group I and II growth and continued up to 630 °C and 9 kbar. We continue to use the growth intervals $\Delta T_I = \Delta T_{II} = 50$ °C and $\Delta T_{III} = 40$ °C for the growth intervals of size groups I, II and III, respectively. The interpretation of the three growth intervals are supported by petrographic observations showing that both group III garnet crystals and the rims of group I and II crystals are poor in ilmenite inclusions, while the cores of group I and II garnet crystals are rich in ilmenite inclusions. An independent test for the growth intervals derived on the basis of the chemistry is also provided by the volumetric proportions of the three size groups in the rock. Garnet makes up about 12% of the rock, which is consistent with the modal contours on Fig. 7(b). In summary, groups I and II appear to have grown over the same temperature interval (with a possible later nucleation of group II than group I) and group III crystals appear to have grown later.

Combining the temperature ranges of the growth intervals from above, with the volumes of a single crystals from each size group (Table 3a) it is now possible to derive growth rates of the crystals. Using the volumes and growth intervals summarised in Table 3a we infer that garnet of groups I, II and III grew at rates of $\bar{g}_I(T) = V_I/\Delta T_I = 18$ mm^3/°C, $\bar{g}_{II}(T) = V_{II}/\Delta T_{II} = 3.6$ mm^3/°C and $\bar{g}_{III}(T) = V_{III}/\Delta T_{III} = 0.1$ mm^3/°C. In order to convert these growth rates per temperature into temporal growth rates, it is necessary to know the heating rate of the rock. While little is known about the rates of heating during the Eoalpine event, Neubauer *et al.* (1995) constrained details of the cooling path of the Gleinalm complex. They derived cooling rates of 10 °C Myr^{-1} using dating of a series of geochronological systems with successively lower closure temperatures. The Eoalpine event is generally known as a regional metamorphic event with continuous *P–T* path. Models for regional metamorphism suggest that such metamorphic events are characterised by similar heating and cooling rates on the heating and cooling path, respectively (e.g. England & Thompson, 1984). It is therefore suggested that heating rates during the Eoalpine metamorphic event were also of the order of $h = 10$ °C Myr^{-1} and discuss the robustness of our interpretation to this assumption later. Using this heating rate, the temporal growth rates of three size groups are: $\bar{g}_I(t) = h/\Delta T_I = 180$ mm^3/Myr, $\bar{g}_{II}(t) = hV_{II}/\Delta T_{II} = 36$ mm^3/Myr and $\bar{g}_{III}(t) = hV_{III}/\Delta T_{II} = 1$ mm^3/Myr (see eq. (2)). The volumetric growth is assumed to be linear in the temperature interval considered.

STRAIN RATE ESTIMATES

In order to use some of the information on growth and rotation rates of porphyroblasts to estimate strain rate, a garnet crystal was selected from size group I, as this is the only size group for which the nucleation and growth interval may be constrained without too much ambiguity. The chosen crystal has the size $L = \bar{L}_1 = 12$ mm, it is spherical in shape and it is far enough from neighbouring crystals so that eq. (1) may be used to describe its rotation rate. A section of this crystal was used that is in the lineation and normal to foliation and is central to the crystal (Fig. 9a). For the estimates, the shape of the spiral inclusion trail in this garnet is used along with estimates for the volumetric growth rate from above. In order to know the radial surface of the crystal as a function of time it is necessary to convert the volumetric growth rates from above into radial growth rate. This may be done by using:

$$V_{(t)} = \frac{4R_{(t)}^3\pi}{3} = \int g_{(t)}dt \tag{4}$$

where $R(t)$ is the radius of the crystal as a function of time. If the growth rate is constant (which it need not be – see below) then eq. (4) is easy to integrate. Using eq. (2) this gives:

$$V_{(t)} = h\frac{V}{\Delta T}\cdot t \tag{5}$$

Substituting eq. (3) into eq. (5) and then into the left hand side of eq. (4) and solving for $R(t)$ gives:

$$R_{(t)} = \left(\frac{L}{2}\right)\cdot\sqrt[3]{\frac{ht}{\Delta T}}. \tag{6}$$

Strain rates were then inferred by assuming that they are given directly by the change in angle of the inclusion trail with time. This was measured by measuring the change in angle $d\alpha$ with radius and multiplying with the time derivative of eq. (6):

$$\dot{\omega} = \frac{d\alpha}{dt} = \frac{d\alpha}{dR}\frac{dR}{dt}. \tag{7}$$

Strain rates were then derived by substituting the derived rotation rate into eq. (1). Note that all the estimates below pertain only to the simple shear component of the overall strain rate tensor, as there is no porphyroblast rotation in response to the pure shear component (as our porphyroblasts are spherical; see Figs 1 & 5).

Figure 9(b) shows a schematic sketch of the garnet crystal from Fig. 9(a) which is radially contoured for

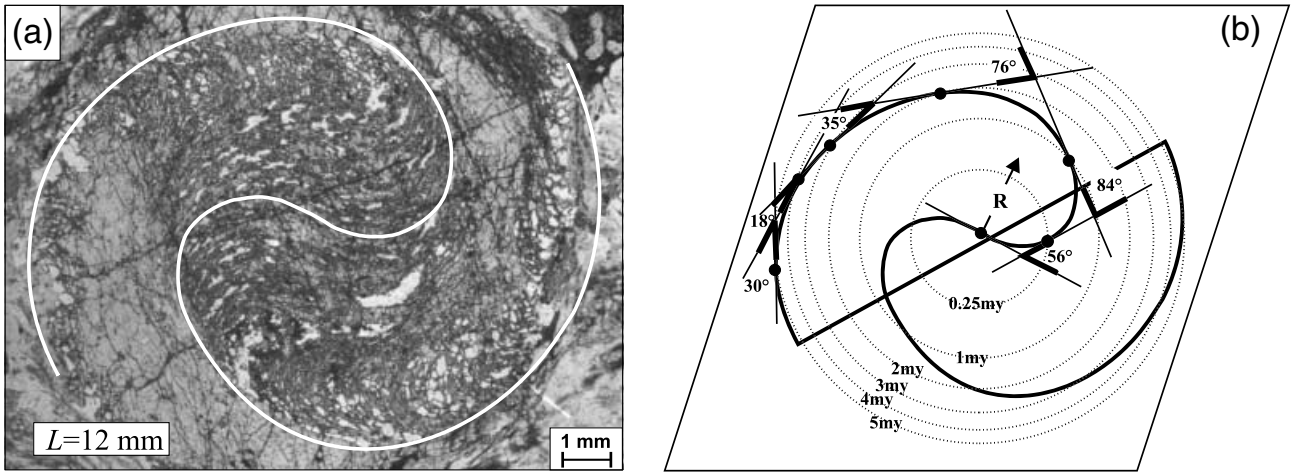

Fig. 9. (a) Spiral inclusion trails in a garnet from size group 1 shown from a section cut central to the crystal, parallel to lineation and normal to foliation. This crystal is more than 2 L from the next crystal so that we use eq. (1) to describe its rotation rate. (b) Schematic sketch of the crystal from (a) showing its spiral trail and volumetric growth contours assuming volumetric growth rate is constant. Circles in the garnet show garnet radius at different times. α is the angle of inclusion trail rotation per volume percent growth. The intersections between the inclusion trail and the growth contours (black dots) are used to construct tangents to the inclusion trail and therefore to measure the angle of rotation during time and garnet growth.

the position of the crystal surface during constant volumetric growth. For practical reasons, finite angle changes $\Delta\alpha$ are shown at discrete intervals of R which were calculated for different time steps using eq. (6) (rather than taking the analytical approach of eq. (7)). Table 3b shows the derived strain rates for an assumed heating rate of $h = 10$ °C Myr^{-1} and a growth interval of $\Delta T_I = 50$ °C (see above). It may be seen that these estimates suggest a strain rate decrease from $\dot{\gamma} = 2.5 \times 10^{-13}$ s^{-1} during the first growth stage to $\dot{\gamma} = 3.3 \times 10^{-14}$ s^{-1} for the last growth stage. The mean strain rate for the whole growth interval is $\dot{\gamma} = 6.6 \times 10^{-14}$ s^{-1}.

However, garnet growth may not be governed by heat flow constraints, so that crystal growth may not be volumetrically constant, even at a constant heating rate. Rather, crystal growth may be interface controlled yielding a constant radial growth rate or it may be an isothermal diffusion controlled process during which the radial growth rate decreases with time (e.g. Christensen *et al*., 1994). Both processes may be best approximated by simply assuming constant radial growth rate. In order to test our estimates for this assumption, Table 3c summarises strain rate calculations for the assumption of a constant radial growth rate. The last column shows that this assumption results in a slight increase in the interpreted strain rate during the growth interval. In conclusion, we suggest that knowledge of growth controlling processes is probably not good enough to infer trends in the strain rate change and continue by discussing the derived mean stain rate ($\dot{\gamma} = 6.6 \times 10^{-14}$ s^{-1}) only.

Robustness of estimates and geological relevance

In order to derive strain rates an integrated approach was applied using a range of analytical methods and thermodynamic modelling tools, coupled with are range of assumptions. While it is practically impossible to discuss the effects and errors introduced by all assumptions and methods, we discuss here some of the most important parameters influencing our estimates. These are the assumptions made for the heating rate and those made to construct the pseudosection shown on Fig. 7. Both assumptions concern the interpretation of the growth rate.

Heating rate problems

The calculations presented above were based on an assumed heating rate of $h = 10$ °C Myr^{-1}. Clearly, if the true heating rates were twice or half this value, then the strain rate estimates above would be too large or too small by the same factor, respectively. Considering that at least the rough order of magnitude of heating rates in orogenic processes is usually known, while the order of magnitude of strain rate is not, it may be concluded that our approach is reasonably robust towards the heating rate assumptions. Derived strain rate changes, however, strongly depend on changes of the heating rate with time. In orogenic processes the heating rate decreases (by definition) to zero at the metamorphic temperature peak. Thus, the assumption of $h = 10$ °C Myr^{-1} is likely to be an overestimate for the later part of the prograde evolution. An overestimate of the heating rate during the growth of the garnet rims would result in a decrease of the strain rate estimates for the rims. However, in view of the poorly constrained growth rate (i.e. is it volumetric or radially constant—see above), even during a perfectly constrained thermal history, we suggest that it may be difficult to infer strain rate derivatives.

Pseudosection problems

Thermodynamic pseudosections have been an amazingly successful tool in metamorphic studies predicting metamorphic *P–T* paths, considering the range of assumptions that have to be made to construct them. Critical among these assumptions is the knowledge of the correct bulk composition. Knowing the correct bulk composition is particularly difficult (if not impossible) with rocks where the prograde evolution is preserved by some crystals and which, therefore, cannot be represented by a single bulk composition. Here we refrain from a discussion of the associated problems and refer to Marmo *et al.* (2002) and Stüwe (1997) for a more in-depth discussion of this problem.

Another point critical for the interpretation of the pseudosection used here (Fig. 7) is the potential influence of Mn on the system TiO_2–NCKFMASH. Garnet contains up to 3% MnO (Table 1) and this influence must therefore be evaluated. The effect of Mn on the stability of metapelites was discussed by Mahar *et al.* (1997) and by Tinkham *et al.* (2001). Tinkham *et al.* (2001) showed that garnet growth in the system MnNCKFMASH may commence around 470 °C at 5 kbar (Fig. 7b) which is some 150 °C lower than the onset of garnet growth in KFMASH (where it occurs around 600 °C, 8 kbar in the divariant field Grt–Chl–Bt–Ms-Qtz-H_2O). It is also 50–60 °C lower temperature than the onset of garnet growth in MnKFMASH discussed by Mahar *et al.* (1997). The onset of garnet growth in MnNCKFMASH is parallel to that in TiO_2–NCKFMASH, but at some 40 °C lower temperature. Fortunately, both Mahar *et al.* (1997) and Tinkham *et al.* (2001) have shown that that the addition of components to the simple pelite system KFMASH system does shift the garnet stability field, but largely preserves the sequence and slopes of garnet producing reactions. As the shifts do not change the modal contours by more than a factor of two in the temperature interval considered, the effects of Mn are practically negligible in comparison to the influence of errors in the assumed heating rate (see above). Naturally, they are then also negligible in view of the goal to obtain only an order of magnitude constraint on strain rate. Correspondingly, modal contours on all calculated pseudosections have a largely constant spacing. Thus, derived trend changes in strain rate are more robust towards the pseudosection than they are towards possible changes in the heating rate or the growth controlling process.

Geological relevance

The strain rate derived here were estimated on the basis of the interpretation of a single garnet crystal. Thus they only pertain to the direct environment of the investigated crystal, i.e. to several cubic centimetres of the rock. In view of the inherent heterogeneity of strain it is difficult to extrapolate these results to the strain rate of the whole rock or even to the deformation rates of the Austroalpine as a whole. Nevertheless, we are excited to report that the strain rates derived here are consistent with the inferred tectonic evolution of the Gleinalm complex (Neubauer *et al.*, 1995) and also with some of the few earlier direct measurements of strain rate, namely those of Christensen *et al.* (1994). The Gleinalm Complex evolved during Eoalpine metamorphism (*c.* 80 Ma, Thöni & Jagoutz, 1993) and formed a dome-shaped structure during its exhumation in the early Tertiary at *c.* 50 Ma. Its structural evolution involved shortening to some 50% during this time interval, which is consistent with bulk longitudinal strain rates between 10^{-13} and 10^{-14}. Nevertheless, we emphasise that these longitudinal strain rates on an orogenic scale are very difficult to compare to the shear strain rates derived here on the scale of a single crystal.

CONCLUSIONS

(1) Spiral inclusion trails in garnet porphyroblasts are a potentially useful tool to measure strain rates of rocks on a thin section scale. Albeit subject to potentially large analytical errors, the method allows the derivation of strain rates if the prograde heating evolution of the rock and the growth controlling parameters are known. Using some simple assumptions about these parameters for the Gleinalm complex in the eastern Alps, we derive a mean strain rate of $\dot{\gamma} = 6.6 \times 10^{-14}\ s^{-1}$ for a small volume around a single garnet crystal used for the study. This estimate is consistent with regional geological estimates for the region.

(2) In order to select an appropriate garnet crystal for the strain rate estimates, a full investigation of the relative growth and nucleation history of all crystal size fractions in the investigated rock was performed. Using trace and major element distributions in differently sized crystals, three growth intervals were derived for three different crystal size fractions. These are: size fraction $L = 12$ mm grew between 540 and 590 °C, crystals of size $L = 7$ mm grew between 540 and 590 °C and crystals of size $L = 2$ mm between 590 and 630 °C of the prograde evolution.

(3) The major element distribution was also used in combination with thermodynamic pseudosections in an appropriate model system to constrain the full the prograde evolution of the Gleinalm complex. This is constrained to have evolved from about 540 °C and 7 kbar to a metamorphic peak around 630 °C and 9 kbar.

(4) Spiral inclusion trails in garnet vary dramatically within one thin section in both, direction and curvature. In order to explain this observation, a finite element modelling approach was used to investigate the rotation rate of porphyroblasts as a function of porphyroblast density. The results suggest that rotation rate can typically vary between 25 and 75% of the shear strain but may be even negative if porphyroblasts touch each other.

ACKNOWLEDGEMENTS

This study was supported by the Austrian Academy of Sciences and the FWF (Austrian Science Foundation) P12846-GEO. For trace and major element analyses we acknowledge the support of European Community Access to research Infrastructure action of Improving Human Potential Programme, contract HPRI-CT-1999–00008 awarded to B.J. Wood (EU Geochemical Facility, University of Bristol). For the improvement of our understanding in thermodynamic modelling we gratefully acknowledge C. Carson and R. Powell. We are in debt to L. Evans for her continued software support with the FEM package BASIL. W. Carlson and P. Williams are thanked for their helpful and constructive reviews and D. Robinson is thanked for efficient editorial handling. W. Carlson is thanked particularly for complimenting our study by encouraging us to omit the question mark we had at the end of the title in the original version. For their continued help with analytical work and interesting discussions we thank F. Bernhard, K. Ettinger, A. Proyer, M. Putz and V. Tenczer.

REFERENCES

Barr, T. D. & Houseman, G. A., 1996. Deformation fields around a fault embedded in a non linear ductile medium. *Geophysical Journal of International*, **125,** 473–490.

Bea, F., Montero, P., Garuti, G. & Zacharini, F., 1997. Pressure-Dependance of Rare Earth Elements Distributions in Amphibolite- and Granulite- Grade Garnets. A LA-ICP-MS Study. *Geostandards Newsletter, the Journal of Geostandards and Geoanalysis*, **21,** 253–270.

Bell, T. H., 1985. Deformation partitioning and porphyroblast rotation in metamorphic rocks radical reinterpretation. *Journal of Metamorphic Geology*, **3,** 109–118.

Bell, T. H., Duncan, A. C. & Simmons, J. V., 1989. Deformation partitioning, shear zone development and the role of undeformable objects. *Tectonophysics*, **158,** 163–171.

Bell, T. H., Forde, A. & Hayward, N., 1992a. Do smoothly curved, spiral-shaped inclusion trails signify porphyroblast rotation? *Geology*, **20,** 59–62.

Bell, T. H., Johnson, S. E., Davis, B., Forde, A., Hayward, N. & Wilkins, C., 1992b. Porphyroblast inclusion-trail orientation data: eppure non son girate!. *Journal of Metamorphic Geology*, **10,** 295–307.

Biermeier, C., Stüwe, K. & Barr, T. D., 2001. The rotation rate of cylindrical objects during simple shear. *Journal of Structural Geology*, **23,** 765–776.

Bjornerud, M. G. & Zhang, H., 1994. Rotation of porphyroblasts in non-coaxial deformation: insights from computer simulations. *Journal of Metamorphic Geology*, **12,** 135–139.

Carlson, W. D., 1989. The significance of intergranular diffusion to the mechanism and kinetics of porphyroblast crystallization. *Contributions to Mineralogy and Petrology*, **103,** 1–24.

Carlson, W. D., 1991. Competitive diffusion-controlled growth of porphyroblasts. *Mineralogical Magazine*, **55,** 317–330.

Carlson, W. D., 2002. Scales of disequilibrium and rates of equilibration during metamorphism. *American Mineralogist*, **87,** 185–204.

Carlson, W. D., Denison, C. & Ketcham, R. A., 1995. Controls on the nucleation and growth of porphyroblasts: kinetics from natural textures and numerical models. *Geological Journal of*, **30,** 207–225.

Christensen, J. N., Selverstone, J., Rosenfeld, J. L. & DePaolo, D. J., 1994. Correlation by Rb-Sr geochronology of garnet growth histories from different structural levels within the Tauern Window, Eastern Alps. *Contribution to Mineralogy and Petrology*, **118,** 1–12.

Daniel, C. G. & Spear, F. S., 1999. The clustered nucleation and growth processes of garnet in regional metamorphic rocks from North-west Connecticut, USA. *Journal of Metamorphic Geology*, **17,** 503–520.

Denison, C. & Carlson, W. D., 1997. Three-dimensional quantitative textural analysis of porphyroblasts metamorphic rocks using high-resolution computed X-ray tomography: Part II. Application to natural samples. *Journal of Metamorphic Geology*, **15,** 45–57.

England, P. C. & Thompson, A., 1984. Pressure-temperature-time paths of regional metamorphism I. Heat transfer during the evolution of regions of thickened continental crust. *Journal of Petrology*, **25,** 894–928.

Escuder Viruete, J., Indares, A. & Arenas, R., 2000. P-T paths derived from garnet growth zoning in an extensional setting; an example from the Tormes gneiss dome (Iberian Massif, Spain). *Journal of Petrology*, **41,** 78.

Finlay, C. A. & Kerr, A., 1987. Evidence for difference in growth rate among garnets in pelitic schists from northern Sutherland, Scotland. *Mineralogical Magazine*, **51,** 569–576.

Ghosh, S. K. & Ramberg, H., 1976. Reorientation of inclusions by combination of pure shear and simple shear. *Tectonophysics*, **34,** 1–70.

Hickey, K. A. & Bell, T. H., 1999. Behaviour of rigid objects during deformation and metamorphism: a test using schists from the Bolton syncline, Conneticut, USA. *Journal of Metamorphic Geology*, **17,** 211–228.

Hickmott, D. D. & Shimizu, N., 1990. Trace element zoning in garnet from the Kwoiek area, British Columbia; disequilibrium partitioning during garnet growth? *Contributions to Mineralogy and Petrology*, **104,** 619–630.

Hickmott, D. D., Shimizu, N., Spear, F. S. & Selverstone, J., 1987. Trace-element zoning in a metamorphic garnet. *Geology*, **15,** 573–576.

Hickmott, D. & Spear, F. S., 1992. Major- and trace-element zoning in garnets from calcareous pelites in the NW Shelburne Falls Quadrangle, Massachusetts; garnet growth histories in retrograded rocks. *Journal of Petrology*, **33,** 965–1005.

Holland, T. J. B. & Powell, R., 2001. Calculation of phase relations involving haplogranitic melts using an internally consistent thermodynamic dataset. *Journal of Petrology*, **42,** 673–683.

Jeffrey, G. B., 1922. The motion of ellipsoidal particles immersed in a viscous fluid. *Proceedings of the Royal Society of London, Series A*, **102,** 161–179.

Johnson, S. E. & Bell, T. H., 1996. How useful are 'millipede' and other similar porphyroblast microstructures for determining synmetamorphic deformation histories? *Journal of Metamorphic Geology*, **14,** 15–28.

Jones, K. A., Morgan, G. J. & Galway, A. K., 1972. The significance of the size distribution function of crystals formed in metamorphic reactions. *Chemical Geology*, **9,** 137–143.

Kretz, R., 1973. Kinetics of the crystallization of garnet at two localities near Yellowknife. *Canadian Mineralogist*, **12,** 1–20.

Kretz, R., 1974. Some models for the rate of crystallization of garnet in metamorphic rocks. *Lithos*, **7,** 123–131.

Kretz, R., 1983. Symbols for rockforming minerals. *American Mineralogist*, **68,** 277–279.

Kretz, R., 1993. A garnet population in Yellowknife schist, Canada. *Journal of Metamorphic Geology*, **11,** 101–120.

Lanzirotti, A., 1995. Yttrium zoning in metamorphic garnets. *Geochimica et Cosmochimica Acta*, **59,** 4105–4110.

Mahar, E. M., Baker, J. M., Powell, R., Holland, T. J. B. & Howell, N., 1997. The effect of Mn on mineral stability in metapelites. *Journal of Metamorphic Geology*, **15,** 223–238.

Mancktelow, N. S. & Visser, P., 1993. The rotation of garnet porphyroblasts around a single fold, Lukmanier Pass, Central Alps: Reply. *Journal of Structural Geology*, **15,** 1369–1372.

Marmo, B. A., Clarke, G. L. & Powell, R., 2002. Fractionation of bulk rock composition due to porphyroblast growth: effects on eclogite facies mineral equilibria, Pam Peninsula, New Caledonia. *Journal of Metamorphic Geology*, **20,** 151–165.

Masuda, T. & Ando, S., 1988. Viscous flow around rigid spherical body: a hydrodynamical approach. *Tectonophysics*, **148,** 337–346.

Masuda, T. & Mochizuki, S., 1989. Development of snowball structure: numerical simulation of inclusion trails during synkinematic porphyroblast growth in metamorphic rocks. *Tectonophysics*, **170,** 141–150.

Miller, Ch & Thöni, M., 1997. Eo-Alpine eclogitisation of Permian MORB-type gabbros in the Koralpe (Eastern Alps, Austria): new geochronological, geochemical and petrological data. *Chemical Geology*, **137,** 283–310.

Müller, W., Aerden, D. & Halliday, A. N., 2000. Isotopic Dating of Strain Fringe Increments: Duration and Rates of Deformation in shear Zones. *Sciences*, **288,** 2195–2198.

Neubauer, F., Dallmeyer, R. D., Dunkl, I. & Schirnik, D., 1995. Late Cretaceous exhumation of the metamorphic Gleinalm dome, Eastern Alps: kinematics, cooling history and sedimentary response in a sinistral wrench corridor. *Tectonophysics*, **242,** 79–98.

Passchier, C. W., Trouw, A. J., Zwart, H. J. & Vissers, R. L. M., 1992. Porphyroblast rotation: eppur si muove? *Journal of Metamorphic Geology*, **10,** 283–294.

Pearce, N. J. G., Perkins, W. T., Westgate, J. A., Gordon, M. P., Jackson, S. E., Neal, C. R. & Chenery, S. P., 1997. A new compilation of new and published major and trace-element data for NIST SRM-610 and NIST SRM-612 glass reference materials. *Geostandards Newsletter*, **21,** 115–144.

Pfiffner, O. A. & Ramsay, J. G., 1982. Constraints on geological strain rates; arguments from finite strain states of naturally deformed rocks. *Journal of Geophysical Research B*, **87,** 311–321.

Powell, R. & Holland, T. J. B., 1988. An internally consistent thermodynamic dataset with uncertainties and correlations: 3 application to geobarometry worked examples and a computer program. *Journal of Metamorphic Geology*, **6,** 173–204.

Rosenfeld, J. L., 1970. Rotated garnets in metamorphic rocks. [Monograph]. *Geological Society of America, Special Paper*, **129,** 105pp.

Schoneveld, C., 1977. A study of some typical inclusion patters in strongly paracrystalline-rotated garnets. *Tectonophysics*, **39,** 453–471.

Schuster, R. & Thöni, M., 1996. Permian Garnet: Indications for a regional Permian metamorphism in the southern part of the Austroalpine basement units. *Mitteilungen der Österreichischen Mineralogischen Gesellschaft*, **141,** 219–221.

Simpson, C. & De Paor, D. G., 1993. Strain and kinematic analysis in general shear zones. *Journal of Structural Geology*, **15,** 1–20.

Spear, F. S. & Daniel, C. G., 1998. 3-dimensional imaging of garnet porphyroblast sizes and chemical zoning; nucleation and growth history in the garnet zone [Monograph]. *Geological Materials Research*, **1,** 1–48.

Spear, F. S. & Daniel, C. G., 2001. Diffusion control of garnet growth, Harpswell Neck, Maine, USA. *Journal of Metamorphic Geology*, **19,** 179–195.

Stüwe, K., 1997. Effective bulk composition changes due to cooling: a model predicting complexities in retrograde reaction textures. *Contributions to Mineralogy and Petrology*, **129,** 43–52.

Stüwe, K. & Powell, R., 1995. PT paths from modal proportions: application to the Koralm Complex, Eastern Alps. *Contributions to Mineralogy and Petrology*, **119,** 83–93.

Thöni, M. & Jagoutz, E., 1993. Isotopic constraints for eo-Alpine high-P metamorphism in the Austroalpine nappes of the Eastern Alps: bearing on Alpine orogenesis. *Schweizer Mineralogische und Petrographische Mitteilungen*, **73,** 177–189.

Tinkham, D. K., Zuluaga, C. A. & Stowell, H. H., 2001. Metapelite phase equilibria modeling in MnNCKFMASH: The effect of variable Al_2O_3 and MgO/ (MgO + FeO) on mineral stability. *Geological Materials Research*, **3,** 1–42.

Vance, D. & Mahar, E., 1998. Pressure-temperature paths from P-T pseudosections and zoned garnets; potential, limitations and examples from the Zanskar Himalaya, NW India. *Contributions to Mineralogy and Petrology*, **132,** 225–245.

Vance, D. & O'Nions, R. K., 1992. Prograde and retrograde thermal histories from the Central Swiss Alps. *Earth and Planetary Science Letters*, **114,** 113–129.

Visser, P. & Mancktelow, N. S., 1992. The rotation of garnet porphyroblasts around a single fold, Lukmanier Pass, Central Alps. *Journal of Structural Geology*, **14,** 1193–1202.

Williams, P. F. & Jiang, D., 1999. Rotating garnets. *Journal of Metamorphic Geology*, **17,** 367–378.

Williams, P. F. & Schoneveld, C., 1981. Garnet rotation and the development of axial plane crenulation cleavage. *Tectonophysics*, **78,** 307–334.

Yang, P. & Rivers, T., 2001. Chromium and manganese zoning in pelitic garnet and kyanite; spiral, overprint, and oscillatory (?) zoning patterns and the role of growth rate. *Journal of Metamorphic Geology*, **19,** 455–474.

Yang, P., Rivers, T. & Jackson, S. J., 1999. Crystal-chemical and thermal controls on trace-element partitioning between coexisting garnet and biotite in metamorphic rocks from western Labrador. [Monograph] Mineral-scale processes in metamorphic petrology; the Kretz volume;. *Canadian Mineralogist*, **37,** 443–486.

Zeh, A., 2001. Inference of a detailed P-T path from P-T pseudosection using metapelitic rocks of variable composition from a single outcrop, Shackelton Range, Antarctica. *Journal of Metamorphic Geology*, **19,** 329–350.

Received 25 March 2002; revision accepted 15 October 2002.

APPENDIX: ANALYTICAL AND NUMERICAL TECHNIQUE

Major element analysis by *X*RF to calculate Fig. 7 was undertaken at the Department of Applied Geology, Technical University Graz. Major element compositions of mineral assemblages were analysed with the electron scanning microscope at the University of Graz and with the electron microprobe at the University of Bristol. Mineral analysis used for *P–T* estimates and rim to rim traverse analysis in garnet were carried out by using a SEM system (JEOL JSM-6310) under conditions of 5 nA beam current and 15 kV voltage and wavelength-dispersive analysis were carried out under operating conditions of 15 kV and 20 nA beam current by using a JEOL JXA 8600. Mineral formulae were calculated with the program AX (written by T.J.B. Holland 1999, http://www.esc.cam.ac.uk/astaff/holland). Representative microprobe analyses are shown in Table 1. Thermobarometric calculations were then performed by using the software package THERMOCALC (Powell & Holland, 1988) with the thermodynamic data set of Holland & Powell, 2001).

Trace element analyses were undertaken at the University of Bristol laboratory (EU Geochemical Facility) using a VG Elemental Plasma Quad 3 ICP-MS with S-Option. The laser is a VG Laser Probe II, a frequency quadrupled Nd; YAG laser operating at 266 nm (UV). Typical operating conditions are employed a *c.* 15 μm diameter laser beam, repetition rates of between 6 Hz and energies at the sample surface of around 0.05 mJ. Tuning of the

optimum laser and ICP-MS operating conditions is done using 139 La in NIST 610 standard glass. Oxide formation is checked during tuning by monitoring $^{232}Th^{16}O/^{232}Th$ ratio (or UO/U) and is typically < 0.01. NIST 610 and 612 standards are used for external calibration; these are artificial glasses that have been spiked with up to 60 trace elements with nominal concentrations of 500 μg/g and 50 μg/g, respectively. The concentrations used are the preferred averages compiled by Pearce *et al*. (1997). Total analysis times for both standards is between 45 and 60 s, primarily depending on depth constraints; this comprises a 15-s gas blank (measurement of all analysed peaks without firing the laser) followed by firing of the laser for the remainder of the analysis. Typically data acquisition is started between 10 and 15 s after ablation is initiated; this allows the analysis signal to stabilise. The gas blank is subtracted from data acquired during data collection. Internal standardisation, using ^{29}Si, ^{43}Ca or ^{44}Ca, is employed to correct for variations and fluctuations in the signal during the analysis. Other internal standards can be used in particular cases, for example Hf in zircon. The final analyses are checked for the presence of inclusions and either rejected or the analysis time adjusted accordingly. Final data reduction and calculation of unknown concentrations using external standards is carried out offline using a MATLAB-programme which quantifies concentrations, errors and detection limits and which was written by C. Dalpé at the EU Geochemical facility, University of Bristol. The programme calibration were made against the national Institute of Sciences and Technology (NIST) standard reference material (SRM) 610 and 612, which has a nominal abundance of 500 p.p.m. of trace elements concerned (Pearce *et al*., 1997). Ca, whose concentration was previously determined by EMP analysis, was used as an internal standard to correct the differences in ablation yield between samples and the calibration standard.